Metal Bond Strength Regulation Enables Large-scale Synthesis of Intermetallic Nanocrystals for Practical Fuel Cells

Jiashun Liang[1†], Yangyang Wan[2,3†], Houfu Lv[4], Xuan Liu[1], Fan Lv[5], Shenzhou Li[1], Jia Xu[1], Zhi Deng[1], Junyi Liu[3], Siyang Zhang[1], Yingjun Sun[5], Gang Lu[3], Jiantao Han[1], Guoxiong Wang[4], Yunhui Huang[1], Qing Li[1]*, Shaojun Guo[5]*

[1]State Key Laboratory of Material Processing and Die & Mould Technology, School of Materials Science and Engineering; Huazhong University of Science and Technology, Wuhan, Hubei 430074, China.

[2]Institute for Advanced Materials, School of Materials Science and Engineering, Jiangsu University, Zhenjiang, Jiangsu, 212013 China.

[3]Department of Physics and Astronomy, California State University Northridge, Northridge, California 91330, United States.

[4]State Key Laboratory of Catalysis, Dalian Institute of Chemical Physics, Chinese Academy of Sciences, Dalian 116023, China.

[5]School of Materials Science and Engineering, Peking University, Beijing 100871, China.

*Corresponding author. E-mail: qing_li@hust.edu.cn; guosj@pku.edu.cn

†These authors contributed equally to this work

Abstract: The widespread application of proton exchange membrane fuel cells (PEMFCs) requires highly stable oxygen reduction reaction (ORR) electrocatalysts under typical working conditions (*i.e.*, 0.6-1.5 V, pH < 1)[1-3]. Structurally ordered $L1_0$-PtM (M = Fe, Co, Ni, *etc*) intermetallic nanocrystals (iNCs), benefiting from the chemically ordered structure and higher stability, are one of the best electrocatalysts used for PEMFC[4-8]. However, their practical development is greatly plagued by the challenge that high-temperature annealing (> 700 °C) has to be used for realizing disorder-order phase transition (DOPT) due to the high activation barrier (E_a)[9-11], which always leads to severe particle sintering, morphology change, and makes it highly challenging for gram-scale preparation of desirable PtM iNCs. Here, we report a general low-melting-point metal induced bond strength weakening strategy to promote DOPT of PtM (M = Ni, Co, Fe, Cu, Zn) alloy catalysts. We demonstrate that the introduction of Sn can reduce DOPT temperature to a record-low temperature (≤ 450 °C), which enables ten-gram-scale preparation of high-performance $L1_0$-PtM iNCs. X-ray spectroscopic studies, *in-situ* electron microscopy and theoretical calculations reveal that the Sn-facilitated DOPT mechanism at record-low temperature involves the weakened bond strength and reduced E_a *via* Sn doping, the formation and fast diffusion of low coordinated surface free atom, and subsequent $L1_0$ nucleation. Most importantly, the 15% Sn-doped $L1_0$-PtNi iNCs display outstanding performance in H_2-air fuel cells with a world-record peak power density of 1.45 watt *per* centimetre squared for Pt alloy catalysts and less than 25 percent activity loss after 30000 cycles at a quite low cathode Pt loading amount of 0.12 milligram platinum *per* centimetre squared, representing as the most efficient cathodic electrocatalyst for PEMFCs.

Main: $L1_0$-PtM (M = Fe, Co, Ni, *etc*) intermetallic nanocrystals (iNCs) with chemically ordered structures, much more stable than the disordered counterparts due to their lower formation energy (*e.g.* -0.232 eV/atom for ordered $L1_0$-PtFe) and higher cohesive energy,[12-16] have emerged as one of the best electrocatalysts for PEMFC in the past few years.[4-8] Despite their thermodynamically favored structure, $L1_0$-PtM iNCs can not be made by the typical chemical systhesis because there exist a large activation barrier (E_a) for atomic diffusion in PtM NCs due to the intrinsically strong bonding strengths of Pt-Pt and Pt-M (*e.g.*, ~306.7 kJ mol^{-1} for Pt-Pt and 273.7 kJ mol^{-1} for Pt-Ni) and high melting points of Pt and M (*e.g.*, Pt~1768 ℃, Fe~1538 ℃). [17] As a result, high temperature annealing (typically > 600 ℃, Supplementary Table 1) is so far the only effective approach to allow the atomic diffusion and achieve disorder to order phase transition (DOPT) (Supplementary Fig. 1).[9-11] Inspired by the experimental results from metallic materials, the E_a for atomic diffusion and the bond strength is roughly proportional to the equilibrium melting temperature of metals, T_m, (Supplementary Fig. 2). We hypothesize that introducing a third metal with a low melting point (M') can weaken the bond strength and reduce E_a. Herein, we propose a new concept on low-melting-point metal (*i.e.* Sn (231.9 °C), In (156.6 °C), and Ga (29.8 °C)) induced bond strength weakening (LMIBSW) strategy to promote DOPT of PtM (M = Ni, Co, Fe, Cu, Zn) alloy electrocatalysts and universally reduce the DOPT temperature of these PtM NCs to record-low values. The improved DOPT process enables the easy ten gram-scale synthesis of intermetallic PtM NCs with uniform morphology/size and reduced energy consumption, which has never been achieved for PtM iNCs.

The carbon-supported Pt-Ni-M' NCs were prepared by a wet-chemical method, and denoted as $Pt_{50}Ni_{50-x}M'_x/C$ (x = 7, 10, 15, M' = Sn, In, Ga, Supplementary Fig. 3). Transmission electron microscopy (TEM) images (Supplementary Fig. 4 and Supplementary Fig. 5) show that the A1-$Pt_{50}Ni_{35}Sn_{15}$ NCs disperse uniformly with an average diameter of 3.5 ± 0.5 nm. The inter-plane spacings of the lattice fringes are about 0.220 and 0.194 nm (Supplementary Fig. 5b), corresponding to the (111) and (200) facets of A1-Pt-Ni. As a comparison, the particle size of A1-$Pt_{50}Ni_{50}$ NCs is about 8 nm with polyhedral morphology (Supplementary Fig. 6), indicating that the presence of Sn precursor can promote the nucleation of Pt NCs and thereby decrease the particle size. Energy dispersive X-ray (EDX) elemental mappings confirm the uniform distribution of the Pt, Ni and Sn elements in A1-$Pt_{50}Ni_{50}$ and A1-$Pt_{50}Ni_{35}Sn_{15}$ NCs (Supplementary Fig. 7).

The DOPT temperature and E_a are measured by differential scanning calorimetry (DSC) (Fig. 1a and Supplementary Fig. 8). The DOPT of $Pt_{50}Ni_{35}Sn_{15}$ is observed to be exothermic and associated with a single peak at ~410 °C, indicating that DOPT is thermodynamically favored. The DOPT temperature is ~410 °C, ~200 °C lower than that of pure A1-$Pt_{50}Ni_{50}$ (Supplementary Fig. 8). The kinetic transformation activation energy of A1-$Pt_{50}Ni_{35}Sn_{15}$ is calculated using the Kissinger equation to be 199.5 kJ mol^{-1}, much lower than that of A1-$Pt_{50}Ni_{50}$ (294.4 kJ mol^{-1}, Fig. 1b).

X-ray diffraction (XRD) was used to investigate the crystal structure of $Pt_{50}Ni_{50}/C$ and $Pt_{50}Ni_{50-x}Sn_x/C$ (Fig. 1c and Supplementary Fig. 9a). We found that with Sn content increasing, DOPT became more obvious. At high Sn content of 15%, some diffraction peaks at ~32.5° and ~53.9°, corresponding to $L1_0$ structure, appear, comfirming the phase transition from A1 to $L1_0$. Besides, compared to A1-PtNi, the introduction of Sn will lead to the lattice expansion due to the larger atomic radius of Sn. By contrast, A1-$Pt_{50}Ni_{50}/C$ requires a high temparture of 650 °C for DOPT (Fig. 1c). After DOPT, the particle size of $L1_0$-$Pt_{50}Ni_{35}Sn_{15}/C$ NCs can be well maintained (Supplementary Fig. 10), while $L1_0$-$Pt_{50}Ni_{50}/C$ NCs suffers from severe particle agglomeration and grows up to ca. 30 nm after annealing at high temperature of 650 °C for 1 h (Supplementary Fig. 11). When replacing Sn with 15 at.% Ga or In, weak diffraction peaks related to $L1_0$ structure can be also observed after annealing at 450 °C for 1 h (Supplementary Fig. 9b, Supplementary Fig. 12 and Supplementary Fig. 13).

Importantly, such LMIBSW strategy is quite general for doping other low-melting-point metals such as In, Ga into PtM for facile preparation of other $L1_0$-PtM-based (M = Fe, Co, Cu and Zn) iNCs with high ordering degree (> 60%) at record-low temperatures compared to reported $L1_0$-PtM NCs (≤450 °C, Fig. 1d, Fig. 2a, Supplementary Fig. 14-Fig. 23 and Supplementary Table 1)[5,8,11,18-27]. In addition to the wet-chemical synthesis, the proposed LMIBSW can also applied to other synthetic approach such as impregnation-annealing method with lower cost (Supplementary Fig. 22 and Fig. 23), suggesting the generality of this strategy. In particular, based on the proposed LMIBSW strategy, $L1_0$-$Pt_{50}Ni_{35}Sn_{15}$/C catalysts can be easily scaled up for ten-gram-scale production (Supplementary Fig. 24 and Supplementary Fig. 25). To the best of our knowledge, it is the first time that Pt-based iNCs are produced in such a large-scale, while most of the reported Pt-based iNCs were prepared only in milligram-scale[7,11,25,28], emphasizing the significance of LMIBSW strategy for industrial production and practical applications.

Spherical aberration (Cs)-corrected HAADF-STEM and energy dispersive X-ray (EDX) elemental mapping are employed to analyze the ordered structure. The ordered NCs are viewed along the [001] or [110] zone axis (Fig. 1 e, g, i, k). The ordered structure of $L1_0$-$Pt_{50}Ni_{35}Sn_{15}$ NC is clearly indicated by the high (Pt) and low (Ni) Z contrast, and their periodic arrangement along <1-10> and <110> directions (Fig. 1e). *Inset* of Fig. 1e reveals the corresponding fast Fourier transformation (FFT) pattern of this NP, showing the presence of (110) and (1-10) superlattice spots. These features firmly confirm that the A1-$Pt_{50}Ni_{35}Sn_{15}$ NCs can be converted to highly ordered $L1_0$-$Pt_{50}Ni_{35}Sn_{15}$ NCs after annealing at 450 °C, which is the record-low DOPT temperature for Pt-Ni systems to the best of our knowledge (Supplementary Table 1). Periodic bright/dark column structures were also observed for $L1_0$-$Pt_{50}Fe_{45}Sn_5$, $L1_0$-$Pt_{50}Cu_{45}Sn_5$ and $L1_0$-$Pt_{50}Zn_{40}Sn_{10}$ NCs, showing high ordering degree in these NCs. Moreover, EDX elemental mappings show that Pt, M and Sn distribute uniformly within the NCs (Fig. 1f, h, j, l).

The structural evolution of $Pt_{50}Ni_{35}Sn_{15}$ during annealing was monitored by *in-situ* XRD and X-ray adsorption spectrum (XAS). As the annealing temperature rises from room temperature (RT) to 450 °C, the diffraction peaks show a gradual positive shift (Fig. 2b), ascribed to the compression in *c* direction during A1-$L1_0$ transition.[29] In addition, the superlattice peak, corresponding to (110) facet, appears at 400 °C, which indicates the structure transformation, and is consistent with DSC result. Meanwhile, the ordering degree gradually increases from 2.4% to 49.7% as temperature elevates (Fig. 2c). Afterwards, the ordering degree maintains at ~76 % after holding 60 min at 450 °C, implying the accomplishment of DOPT. Remarkably, the particle size, calculated from Debye-Scherrer equation, maintains at ~3.5 nm during the whole annealing process, demonstrating the merits of our LMIBSW strategy.

The local structure of $Pt_{50}Ni_{35}Sn_{15}$/C during DOPT was investigated by extended X-ray absorption fine structure (EXAFS) and atomic pair distributed function (PDF). In accordance with *in-situ* XRD results, decrease in Pt-Pt distance ($d_{Pt\text{-}Pt}$) is observed upon heating (Fig. 2d). The $d_{Pt\text{-}Pt}$ reduces to 2.701 Å after annealing at 450 °C for 1 h (Supplementary Fig. 26 and Supplementary Table 2). In addition, the average coordination number of Pt-Pt ($CN_{Pt\text{-}Pt}$, 4.6 ± 1.51) is larger than $CN_{Pt\text{-}Ni}$ (1.4 ± 0.38) before DOPT (*i.e.*, < 300 °C) (Fig. 2e, Supplementary Fig. 26 and Supplementary Table 2), suggesting that there exist Pt-rich region in the disordered A1-$Pt_{50}Ni_{35}Sn_{15}$. During DOPT, $CN_{Pt\text{-}Pt}$ decreases and $CN_{Pt\text{-}Ni}$ increases as a result of atomic rearrangement and structural ordering (Fig. 2e). Four distinct peaks can be identified in PDF spectra for A1-$Pt_{50}Ni_{35}Sn_{15}$/C and $L1_0$-$Pt_{50}Ni_{35}Sn_{15}$/C, assigned to the first to the fourth coordinate shells (Fig. 2f). Compared to those of A1-$Pt_{50}Ni_{35}Sn_{15}$/C, the peaks of $L1_0$-$Pt_{50}Ni_{35}Sn_{15}$/C show negative shift to some extent, implying a shortened bond length, which agrees well with XRD and EXAFS results. Compared to that of A1-$Pt_{50}Ni_{50}$/C, the smaller CN of A1-$Pt_{50}Ni_{35}Sn_{15}$ (6.0 *vs.* 9.6) suggests the introduction of low-coordinated atoms after Sn doping.

To further uncover the Sn-facilitated DOPT mechanism of $Pt_{50}Ni_{35}Sn_{15}$, the *in-situ* heating HAADF-STEM was employed. Figure 3a shows the structure evolution of a single $Pt_{50}Ni_{35}Sn_{15}$ NC at elevated temperature viewed along <110> direction. The atomic arrangements at 200 °C and 300 °C indicate a disordered A1 structure (Fig. $3a_1$, Supplementary Fig. 27a-c) with some low-coordinated atoms/sites on the surface, while A1-$Pt_{50}Ni_{50}$ reveals a smoother surface (Supplementary Fig. 27d and Supplementary Fig. 28a). At critical temperature (400 °C), some dissociative "free atom" around the NC can be observed, and become more obvious at higher temperature, attributed to fast surface diffusion (Fig. $3a_2$-a_4 and Supplementary Fig. 29). By contrast, no dissociative "free atom" and surface diffusion can be tracked in $Pt_{50}Ni_{50}$ NCs (Supplementary Fig. 28b), indicating slow atomic diffusion and high E_a for $Pt_{50}Ni_{50}$ NCs. In addition, the nucleation and growth of $L1_0$ phase are tracked using fast Fourier transform (FFT) and inverse fast Fourier transform (IFFT) (Supplementary Fig. 30 and Supplementary Fig. 31). With raising the temperature to 450 °C, two weak (110) superlattice spots appear, suggesting the atomic rearrangement and nucleation of $L1_0$ phase (Fig. $3a_3$ and Supplementary Fig. 30d). The IFFT result confirms that the $L1_0$ phase mainly nucleates on (110) facet and exists on the surface of the NP (Supplementary Fig. 31a-c) because the atomic arrangement on (110) facet is less dense compared to (111) and (100) facets (Supplementary Fig. 32). Elevating the temperature leads to a larger area of $L1_0$ phase due to the following growth of $L1_0$ phase (Fig. $3a_4$ and Supplementary Fig. 31d-f). After annealing at 480 °C for 1 h, $L1_0$ phase with high degree of ordering can be obtained (Supplementary Fig. 33).

Besides, the growth of $L1_0$ phase in a single $Pt_{50}Ni_{35}Sn_{15}$ NC at different times was also monitored (Fig. 3b, Supplementary Fig. 34 and Video S1), and presented by the aforementioned Fourier filters. $L1_0$ and A1 mixed phases are observed at the beginning of video recording (Fig. $3b_1$), with a clear $L1_0$/A1 interface observed. With the prolonged annealing time, the $L1_0$ phase grows continuously and becomes highly ordered after holding for 240 s (Fig. $3b_2$-b_4). And no mixing of grain boundary or coalescence of grains is observed due to single $L1_0$ nucleus in this NC. In addition, $Pt_{50}Fe_{45}Sn_5$ also demonstrates the similar transition phenomenon with $Pt_{50}Ni_{35}Sn_{15}$, including fast surface diffusion and nucleation of $L1_0$ phase on (110) surface (Supplementary Fig. 35 and Supplementary Fig. 36). By contrast, no obvious surface free atom and $L1_0$ phase nucleation are observed for A1-$Pt_{50}Ni_{50}$ NCs under the same condition, even at 650 °C (Fig. 3c and Supplementary Fig. 28c).

DFT calculations were performed to provide more insights into M'-promoted DOPT mechanism. We first focus on the correlations between M' (M' = Sn, In, and Ga) type, bond strength and diffusion barrier (E_a) (Fig. 4a). E_a, the sum of vacancy formation energy (E_{vac}) and hopping barrier (E_{hop}), of different systems on (100) surface are calculated (Fig. 4b and Supplementary Table 3). Figure 4b and Supplementary Fig. 37 shows the average E_{vac} of Ni, Pt and M' in Pt-Ni-M', in which the E_{vac} of Ni is the lowest one (0.007 eV for $Pt_{16}Ni_{11}Sn_5$) among Pt, Ni and M'. In contrast to average E_{vac}, the average E_{hop} is not sensitive to the introduction of M' elements (*ca*. 0.86 eV in different Pt-Ni-M', Fig. 4b and Supplementary Fig. 38). Thus, E_a decreases after introducing M', and follows a trend: $Pt_{16}Ni_{11}Sn_5$ (0.875 eV) < $Pt_{16}Ni_{11}Ga_5$ (1.003 eV) < $Pt_{16}Ni_{11}In_5$ (1.025 eV) < $Pt_{16}Ni_{16}$ (1.165 eV). We further take Ni/Sn ratio into consideration (Fig. 4b and Supplementary Fig. 37-Fig. 39). With increasing Sn content, E_a declines as well. These results firmly verify the fact that introducing a third metal M' with a low melting point can reduce E_a and promote DOPT.

We then quantitatively investigate the relationship between bond strength and E_a of Pt-Ni-M' using classical free-electron model. The metallic bond strength is related to the free electrons in alloy systems where decreased number in free electron results in weakened metallic bonds. The electron localization function (ELF) analysis of the studied Pt-Ni-M' systems reveals that the electrons are more localized around the M' atoms, suggesting a decrease in free electrons (Fig. 4c). In accordance, band structure

or density of states (DOS) analysis also reveals decreased free electron after introducing M' (Fig. 4d, Supplementary Fig. 40 and Supplementary Fig. S41), which suggests weakened metallic bonds in Pt-Ni-M'. The bond strength is further quantified using relative metallic bond strength (RMBS, see SI for more details) as descriptor. Fig. 4d shows the relationship between M', number of free electrons, DOS and RMBS. Compared to $Pt_{16}Ni_{16}$, all of Ga, Sn and In doping can reduce the number of free electrons and thus weaken the bond strength of PtNi, especially for Sn doping at ~15 at.%. Specifically, the RMBS reduces by 50% in $Pt_{16}Ni_{11}Sn_5$ system compared to that of $Pt_{16}Ni_{16}$. We find that E_a (as well as E_{vac}) and RMBS follow the same trend in the studied systems, suggesting that there will be the correlation between these parameters. Interestingly, a linear relation between E_a (as well as E_{vac} and E_{hop}) and RMBS can be obtained after plotting the corresponding parameters, which can be expressed as follows (Fig. 4e):

$$E_a = 0.54\text{RMBS} + 0.61$$
$$E_{hop} = -0.03\text{RMBS} + 0.88$$
$$E_{vac} = 0.57\text{RMBS} - 0.27$$

These results unambiguously demonstrate the strong positive correlation between bond strength and atomic diffusion, in which stronger bond strength leads to harder diffusion. We also calculate the average E_a on (100), (110) and (111) facets. The average E_a on (110) facet is merely 0.695 eV, 0.18 eV and 0.44 eV lower than those on (100) and (111) facets, respectively (Supplementary Table 4). Thus, DOPT will be initiated on (110) facet, in accordance with HAADF-STEM observations. In these regards, DFT results well explain the experimental observations that Sn doping can effectively facilitate the atomic diffusion and lower DOPT temperature *via* weakening the bond strength and reducing E_a.

Besides the above analysis of DOPT kinetics, we also calculate the DOPT driving force, a thermodynamic descriptor of $L1_0$-PtNiM' and $L1_0$-PtNi (Supplementary Fig. 42). Notably, introducing all of three M' can increase the driving force of PtNiM' compared to that of PtNi. The driving force increases from 1.45 eV for $Pt_{16}Ni_{16}$ to 2.66 eV for $Pt_{16}Ni_{11}Sn_5$. Therefore, DFT calculations demonstrate that low-melting-point metal M' doping, in particular Sn doping, can have a good opportunity for promoting A1-$L1_0$ transition of PtM alloys not only by kinetic control, but also by thermodynamic regulation. Therefore, X-ray spectroscopy, STEM results, DFT calculations uncover that the M'-promoted DOPT mechanism consists of: (i) bond strength weakening and E_a decline triggered by M' doping; (ii) formation and diffusion of low-coordinated surface free atoms as a result of reduced E_a; (iii) surface diffusion induced nucleation of $L1_0$ phase on (110) surface at low temperatures; (iv) continuous growth of $L1_0$ phase accompanied with lattice compression until forming highly ordered structures (Fig. 4f).

We evaluated the ORR activity and stability of the obtained NCs. A1-$Pt_{50}Ni_{50}$/C and $L1_0$-$Pt_{50}Ni_{50}$/C with small particle size were prepared as reference (Supplementary Fig. 43). Cyclic voltammetry (CVs) results reveal that the electrochemically active surface areas (ECSAs) of A1-$Pt_{50}Ni_{35}Sn_{15}$/C (58.7 m^2 g_{Pt}^{-1}) and $L1_0$-$Pt_{50}Ni_{35}Sn_{15}$/C (58.6 m^2 g_{Pt}^{-1}) are comparable to that of Pt/C (57.2 m^2 g_{Pt}^{-1}) (Supplementary Fig. 44). Figure 5a and Supplementary Fig. 45 reveals the ORR polarization curves of the studied catalysts. $L1_0$-$Pt_{50}Ni_{35}Sn_{15}$/C demonstrates the best ORR activity with the most positive half-wave potential ($E_{1/2}$) of 0.952 V *vs.* RHE and highest mass activity (MA) of 1.80 A mg_{Pt}^{-1} and specific activity (SA) of 3.08 mA cm^{-2} (Fig. 5b). DFT was used to calculate the adsorption energy of oxygen (ΔE_O, a descriptor for ORR activity) on Pt(111) surface, which also suggests the same trend that $L1_0$-$Pt_{50}Ni_{35}Sn_{15}$/C has the best ORR activity (Supplementary Fig. 46). Besides, $L1_0$-$Pt_{50}Ni_{35}Sn_{15}$/C demonstrates an excellent stability by showing only 4 mV loss in $E_{1/2}$ after 30,000 potential cycles (Supplementary Fig. 47 and Supplementary Fig. 48), respectively. By contrast, A1-$Pt_{50}Ni_{35}Sn_{15}$/C and A1-$Pt_{50}Ni_{50}$/C suffer from 13 mV and 30 mV loss in in $E_{1/2}$ after 20,000 potential cycles, respectively (Supplementary Fig. 49). The enhanced stability of $L1_0$-$Pt_{50}Ni_{35}Sn_{15}$/C can be

ascribed to the ordered structure that stabilizes Ni from dissolution, and Sn doping that reduces the surface energy (Supplementary Fig. 50)

We screened the developed $L1_0$-$Pt_{50}Ni_{35}Sn_{15}$/C catalyst in PEMFCs. $L1_0$-$Pt_{50}Ni_{35}Sn_{15}$/C displays much higher current density than Pt/C and A1-$Pt_{50}Ni_{50}$/C in kinetic region in H_2-O_2 test (V > 0.7 V, Supplementary Fig. 48), suggesting the best intrinsic ORR activity. Impressively, $L1_0$-$Pt_{50}Ni_{35}Sn_{15}$/C achieves an initial MA of 0.6 A mg_{Pt}^{-1} at 0.9 $V_{iR\text{-free}}$, about 2.3 times and 3.3 times higher than those of A1-$Pt_{50}Ni_{50}$/C (0.27 A mg_{Pt}^{-1}) and commercial Pt/C (JM 20%, 0.18 A mg_{Pt}^{-1}), respectively (Fig. 5d). Noteworthy, $L1_0$-$Pt_{50}Ni_{35}Sn_{15}$/C demonstrates extraordinarily high durability in PEMFC cathode. After 30,000 voltage cycles from 0.6 to 0.95 V, $L1_0$-$Pt_{50}Ni_{35}Sn_{15}$/C still delivers a high MA of 0.46 A mg_{Pt}^{-1}, with a MA retention as high as 76.6 % (Fig. 5f). By contrast, Pt/C catalyst suffers from 77.8% activity loss after 30,000 cycles (Supplementary Fig. 49). Both initial MA and stability of $L1_0$-$Pt_{50}Ni_{35}Sn_{15}$/C surpass the DOE 2025 targets of MA (0.44 A mg_{Pt}^{-1}) and MA loss (< 40% after 30,000 cycles), and outperforms most of the reported electrocatalysts (Supplementary Table 5)[7,20,28,32], showing great potential for PEMFC application.

The excellent membrane electrode assembly (MEA) performance of $L1_0$-$Pt_{50}Ni_{35}Sn_{15}$/C was also observed under practical H_2-air conditions. As shown in Fig. 5c, the $L1_0$-$Pt_{50}Ni_{35}Sn_{15}$/C catalyst delivers much higher current density than A1-$Pt_{50}Ni_{50}$/C and commercial Pt/C in the typical operating voltage range (>0.6 V), achieving a high current density of 2.1 A cm^{-2} at 0.6 V. Notably, the $L1_0$-$Pt_{50}Ni_{35}Sn_{15}$/C catalyst reveals the highest peak power density of 1.45 W cm^{-2} at a low Pt loading of 0.12 mg_{Pt} cm^{-2} (Fig. 5d), outperforming those reported for intermetallic catalysts such as Pt_1Co_1-IMC@Pt (1.23 W cm^{-2})[7], PtCo i-NPs (1.08 W cm^{-2})[11] and Pt_3Co/Co-N-C (1.05 W cm^{-2})[32], and representing the most active electrocatalysts among the reported work (Supplementary Table 5)[7,20,28,32].

We also evaluate the rated power of the MEAs as suggested by DOE (94 °C, 0.67 V), which is another important parameter directly reflecting the performance of practical fuel cells under working conditions, nevertheless, rarely reported. Remarkably, the $L1_0$-$Pt_{50}Ni_{35}Sn_{15}$/C catalyst demonstrates a rated power density of 1.03 W cm^{-2} at 0.67 V, meeting DOE target (1 W cm^{-2}) and nearly twice that of commercial Pt/C (Supplementary Fig. 50). After 30,000 voltage cycles, our $L1_0$-$Pt_{50}Ni_{35}Sn_{15}$/C catalyst shows negligible performance loss under H_2-air condition (Fig. 5e and 5f). More specifically, $L1_0$-$Pt_{50}Ni_{35}Sn_{15}$/C retains 84.9 % of the initial peak power density and 77.1% of the rated power density, and show the voltage loss of only 25 mV at 0.8 A cm^{-2} (exceeding the DOE 2025 target of <30 mV) (Supplementary Fig. 51).

References

1 Fan, J. T. *et al.* Bridging the gap between highly active oxygen reduction reaction catalysts and effective catalyst layers for proton exchange membrane fuel cells. *Nat. Energy* **6**, 475-486 (2021).

2 Cullen, D. A. *et al.* New roads and challenges for fuel cells in heavy-duty transportation. *Nat. Energy* **6**, 462-474 (2021).

3 Luo, M. C. *et al.* PdMo bimetallene for oxygen reduction catalysis. *Nature* **574**, 81-85 (2019).

4 Li, Q. *et al.* New Approach to Fully Ordered fct-FePt Nanoparticles for Much Enhanced Electrocatalysis in Acid. *Nano Lett.* **15**, 2468-2473 (2015).

5 Du, X., He, Y., Wang, X. & Wang, J. Fine-grained and fully ordered intermetallic PtFe catalysts with largely enhanced catalytic activity and durability. *Energy Environ. Sci.* **9**, 2623-2632 (2016).

6 Liang, J. *et al.* Tungsten-Doped $L1_0$-PtCo Ultrasmall Nanoparticles as a High-Performance Fuel Cell Cathode. *Angew. Chem. Int. Ed.* **58**, 15471-15477 (2019).

7 Cheng, Q. *et al.* High-loaded sub-6 nm Pt1Co1 intermetallic compounds with high-efficient performance expression in PEMFCs. *Energy Environ. Sci.* **15**, 278-286 (2021).
8 Wang, T. *et al.* Sub‐6 nm Fully Ordered $L1_0$-Pt-Ni-Co Nanoparticles Enhance Oxygen Reduction via Co Doping Induced Ferromagnetism Enhancement and Optimized Surface Strain. *Adv. Energy Mater.* **9**, 1803771 (2019).
9 Zhou, J. H. *et al.* Observing crystal nucleation in four dimensions using atomic electron tomography. *Nature* **570**, 500-503 (2019).
10 Alloyeau, D. *et al.* Size and shape effects on the order-disorder phase transition in CoPt nanoparticles. *Nat. Mater.* **8**, 940-946 (2009).
11 Yang, C. L. *et al.* Sulfur-anchoring synthesis of platinum intermetallic nanoparticle catalysts for fuel cells. *Science* **374**, 459-464 (2021).
12 Yan, Y. C. *et al.* Intermetallic Nanocrystals: Syntheses and Catalytic Applications. *Adv. Mater.* **29**, 1605997 (2017).
13 Liang, J. S. *et al.* Atomic Arrangement Engineering of Metallic Nanocrystals for Energy-Conversion Electrocatalysis. *Joule* **3**, 956-991 (2019).
14 Zhou, M., Li, C. & Fang, J. Y. Noble-Metal Based Random Alloy and Intermetallic Nanocrystals: Syntheses and Applications. *Chem Rev* **121**, 736-795 (2021).
15 Wang, D. L. *et al.* Structurally ordered intermetallic platinum-cobalt core-shell nanoparticles with enhanced activity and stability as oxygen reduction electrocatalysts. *Nat. Mater.* **12**, 81-87 (2013).
16 Bu, L. Z. *et al.* Biaxially strained PtPb/Pt core/shell nanoplate boosts oxygen reduction catalysis. *Science* **354**, 1410-1414 (2016).
17 Porter, D. A. & Easterling, K. E. *Phase transformations in metals and alloys (revised reprint)*. (CRC press, 2009).
18 Li, J. *et al.* Fe Stabilization by Intermetallic $L1_0$-FePt and Pt Catalysis Enhancement in $L1_0$-FePt/Pt Nanoparticles for Efficient Oxygen Reduction Reaction in Fuel Cells. *J. Am. Chem. Soc.* **140**, 2926-2932 (2018).
19 Chen, H. *et al.* Coalescence in the Thermal Annealing of Nanoparticles: An in Situ STEM Study of the Growth Mechanisms of Ordered Pt-Fe Nanoparticles in a KCl Matrix. *Chem Mater* **25**, 1436-1442 (2013).
20 Zhao, X. R. *et al.* High-Performance Nitrogen-Doped Intermetallic PtNi Catalyst for the Oxygen Reduction Reaction. *ACS Catal.* **10**, 10637-10645 (2020).
21 Kim, H. Y. *et al.* Self-Supported Mesostructured Pt-Based Bimetallic Nanospheres Containing an Intermetallic Phase as Ultrastable Oxygen Reduction Electrocatalysts. *Small* **12**, 5347-5353 (2016).
22 Zhao, X. R. *et al.* Rhombohedral Ordered Intermetallic Nanocatalyst Boosts the Oxygen Reduction Reaction. *ACS Catal.* **11**, 184-192 (2021).
23 Kim, H. Y. *et al.* Intermetallic PtCu Nanoframes as Efficient Oxygen Reduction Electrocatalysts. *Nano Lett.* **20**, 7413-7421 (2020).
24 Gong, M. X. *et al.* Structure evolution of PtCu nanoframes from disordered to ordered for the oxygen reduction reaction. *Appl. Catal. B-Environ.* **282**, 119617 (2021).
25 Qi, Z. Y. *et al.* Sub-4 nm PtZn Intermetallic Nanoparticles for Enhanced Mass and Specific Activities in Catalytic Electrooxidation Reaction. *J. Am. Chem. Soc.* **139**, 4762-4768 (2017).
26 Liang, J. S. *et al.* Biaxial Strains Mediated Oxygen Reduction Electrocatalysis on Fenton Reaction Resistant $L1_0$-PtZn Fuel Cell Cathode. *Adv. Energy Mater.* **10**, 2000179 (2020).
27 Han, A. J. *et al.* Isolating contiguous Pt atoms and forming Pt-Zn intermetallic nanoparticles to regulate selectivity in 4-nitrophenylacetylene hydrogenation. *Nat. Commun.* **10**, 3787 (2019).
28 Li, J. *et al.* Hard-Magnet $L1_0$-CoPt Nanoparticles Advance Fuel Cell Catalysis. *Joule* **3**, 124-135 (2019).
29 Zhang, S. *et al.* Tuning Nanoparticle Structure and Surface Strain for Catalysis Optimization.

J. Am. Chem. Soc. **136**, 7734-7739 (2014).
30 Strasser, P. *et al.* Lattice-strain control of the activity in dealloyed core-shell fuel cell catalysts. *Nat. Chem.* **2**, 454-460 (2010).
31 Luo, M. C. & Guo, S. J. Strain-controlled electrocatalysis on multimetallic nanomaterials. *Nat. Rev. Mater.* **2**, 17059 (2017).
32 Chong, L. *et al.* Ultralow-loading platinum-cobalt fuel cell catalysts derived from imidazolate frameworks. *Science* **362**, 1276-1281 (2018).

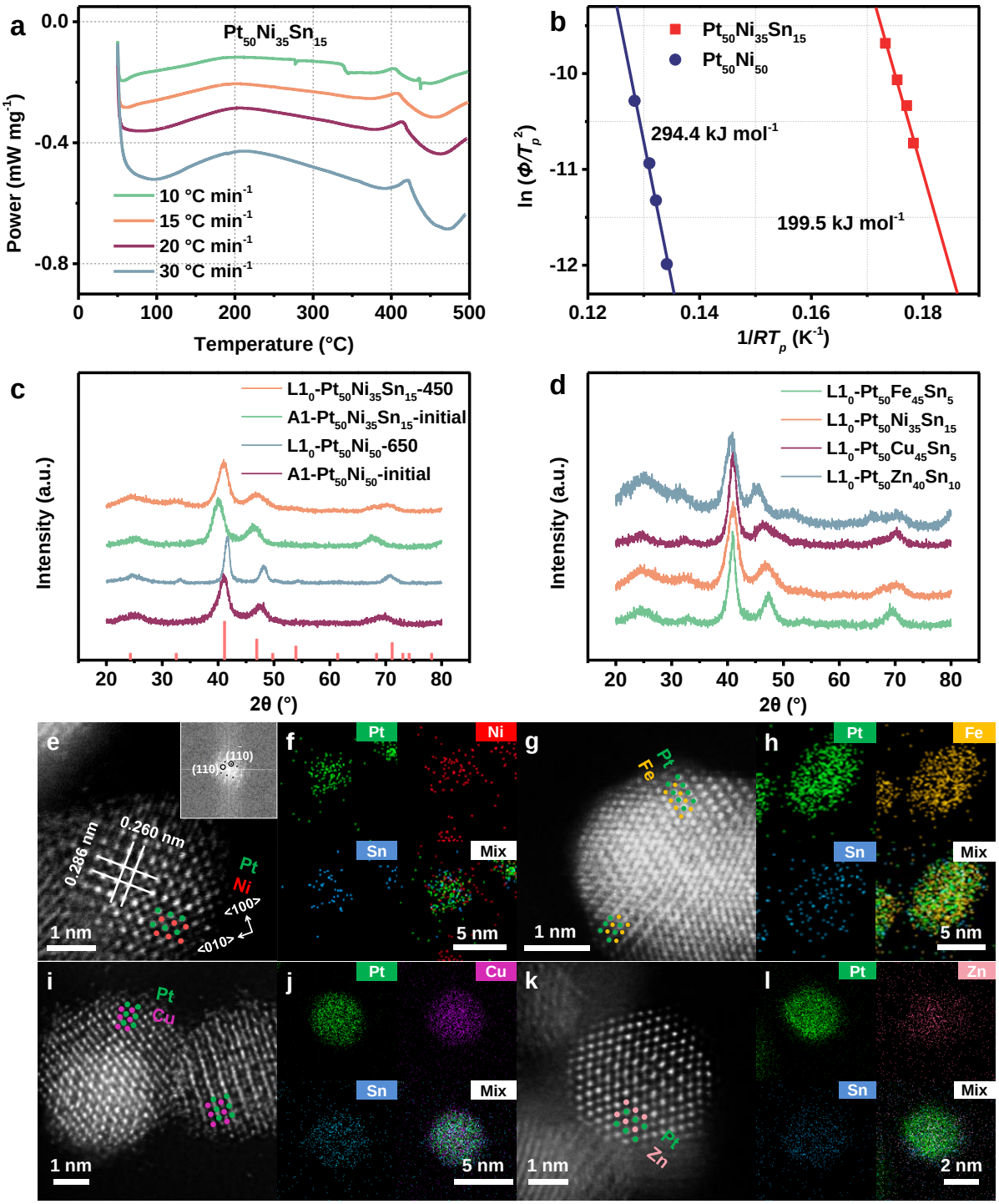

Fig. 1 | Structural characterizations of $Pt_{50}M_{50-x}Sn_x$. a, DSC spectra of $Pt_{50}Ni_{35}Sn_{15}$/C at different heating rate. **b,** E_a of $Pt_{50}Ni_{35}Sn_{15}$/C and $Pt_{50}Ni_{50}$/C calculated using the Kissinger equation. **c,** XRD patterns of $L1_0$-$Pt_{50}Ni_{35}Sn_{15}$/C, A1-$Pt_{50}Ni_{35}Sn_{15}$/C, $L1_0$- $Pt_{50}Ni_{50}$/C and A1- $Pt_{50}Ni_{50}$/C. **d,** XRD patterns of $L1_0$-$Pt_{50}M_{50-x}Sn_x$/C (M = Fe, Ni, Cu, Zn). **e, g, i, k,** Atomic-resolution HAADF-STEM image of **(e)** $L1_0$-$Pt_{50}Ni_{35}Sn_{15}$, **(g)** $L1_0$-$Pt_{50}Fe_{45}Sn_5$, **(i)** $L1_0$-$Pt_{50}Cu_{45}Sn_5$ and **(k)** $L1_0$-$Pt_{50}Zn_{40}Sn_{10}$ NC. **f, h, j, l,** EDX-elemental mappings of **(f)** $L1_0$-$Pt_{50}Ni_{35}Sn_{15}$, **(h)** $L1_0$-$Pt_{50}Fe_{45}Sn_5$, **(j)** $L1_0$-$Pt_{50}Cu_{45}Sn_5$ and **(l)** $L1_0$-$Pt_{50}Zn_{40}Sn_{10}$ NCs.

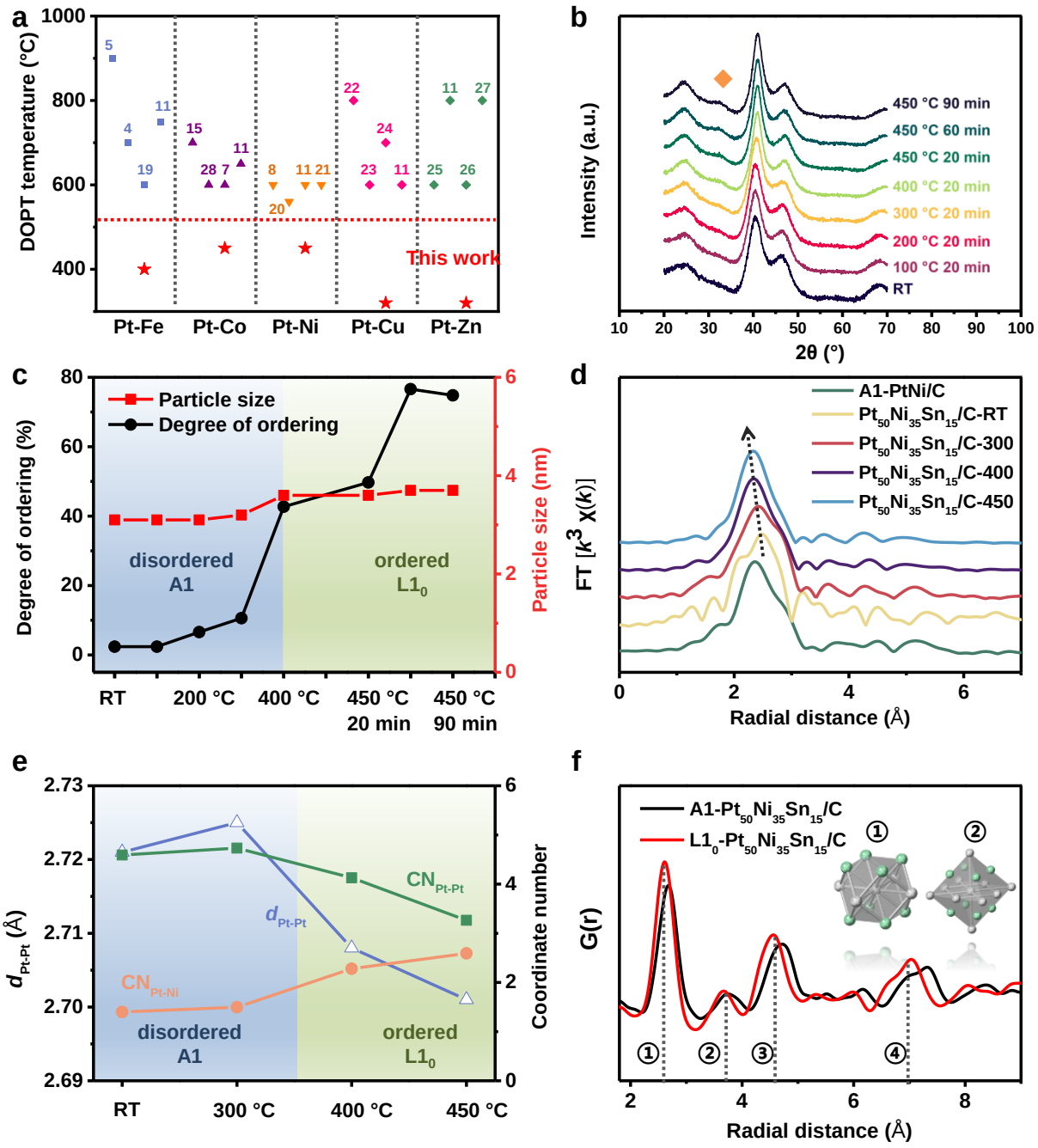

Fig. 2 | X-ray spectroscopy of $Pt_{50}Ni_{35}Sn_{15}$/C NCs during phase transition process. a, Comparison of DOPT temperature of our Pt-M systems and reported works. **b,** *In-situ* XRD patterns of $Pt_{50}Ni_{35}Sn_{15}$/C annealed at different temperature. **c,** Ordering degree and particle size as a function of annealing process. **d,** Pt L_3 k^3-weighted FT-EXAFS spectra of $Pt_{50}Ni_{35}Sn_{15}$/C annealed at different temperature. **e,** d_{Pt-Pt}, CN_{Pt-Pt} and CN_{Pt-Ni} as a function of annealing process. **f,** PDF spectra of A1-$Pt_{50}Ni_{35}Sn_{15}$/C and L1$_0$-$Pt_{50}Ni_{35}Sn_{15}$/C. *Insets* are the atomic models of first and second coordinate shells.

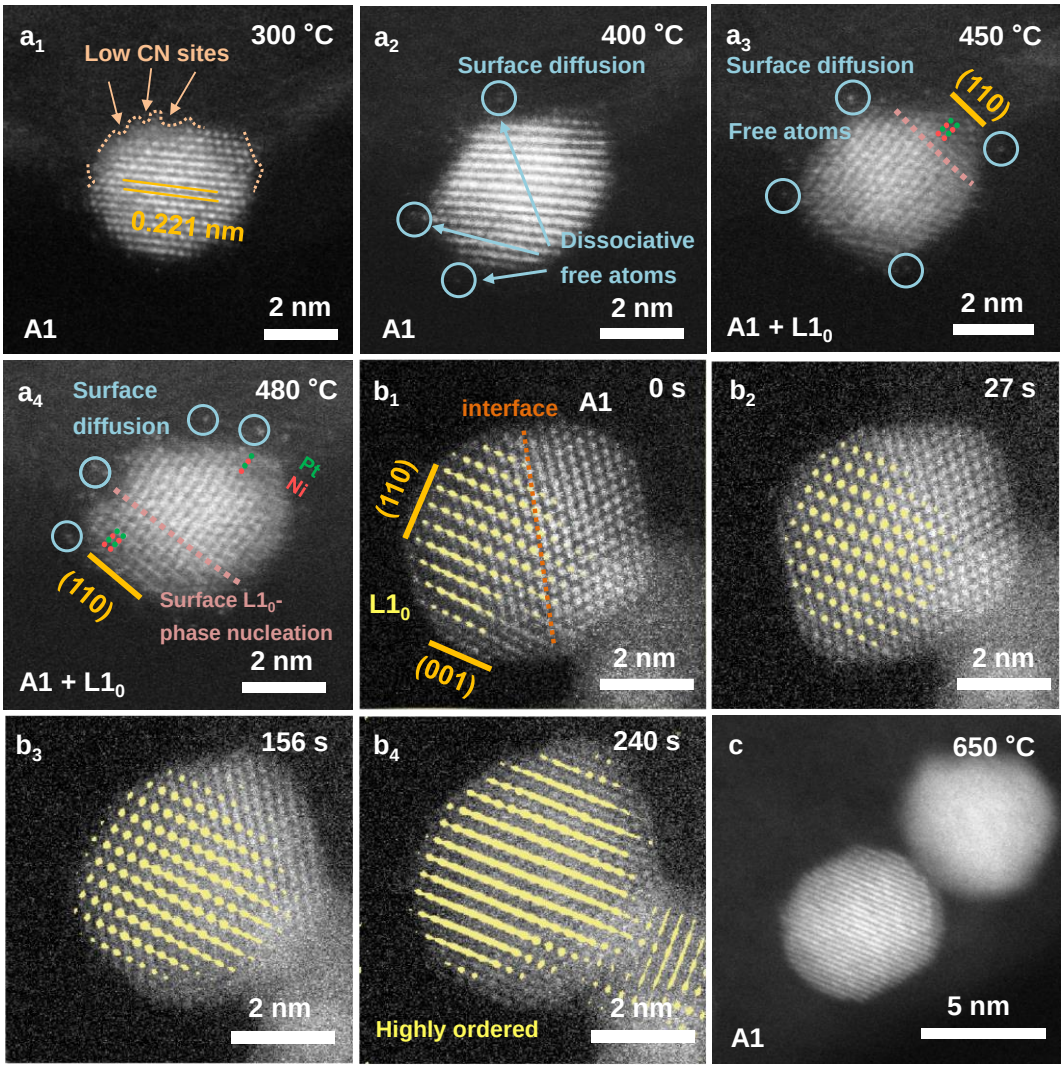

Fig. 3 | *In-situ* heating HAADF-STEM images of $Pt_{50}Ni_{35}Sn_{15}$ and $Pt_{50}Ni_{50}$ NCs during phase transition process. a, $Pt_{50}Ni_{35}Sn_{15}$ NC annealed at elevated temperatures. **b,** $Pt_{50}Ni_{35}Sn_{15}$ NC annealed at 480 °C for different times. **c,** $Pt_{50}Ni_{50}$ NCs annealed at 650 °C.

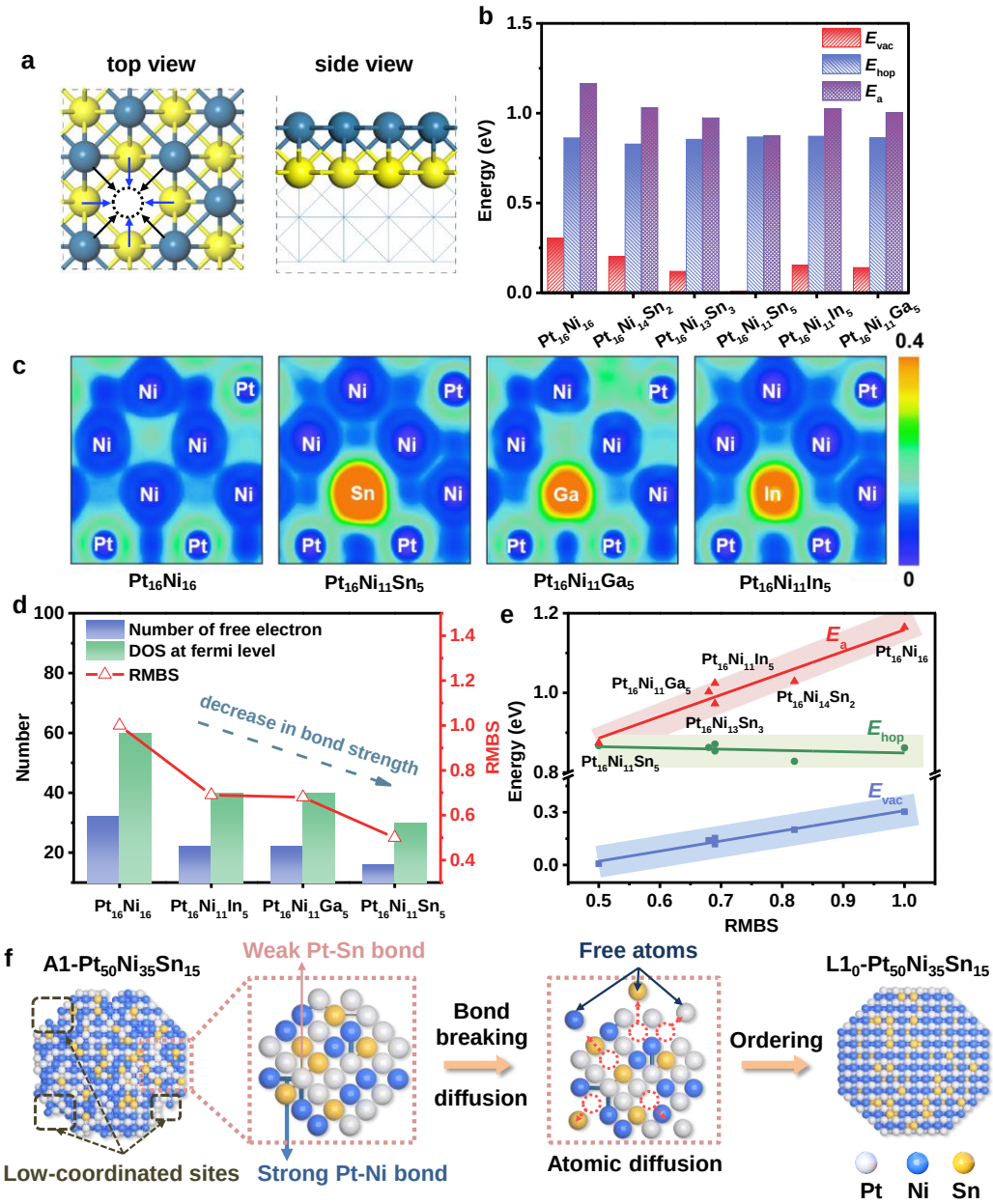

Fig. 4 | Mechanism of Sn-facilitated DOPT process. a, Atomic model for DFT calculations, where gray blue sphere and yellow sphere represent surface and sub-surface atoms, respectively. **b,** Vacancy formation energy (E_{vac}), vacancy hoping energy (E_{hop}) and activation barrier (E_a) of Pt-Ni-M'. **c,** The two-dimensional display of electron localization function (ELF) analysis of corresponding Pt-Ni-M' systems. **d,** Statistic of the number of free electrons, electron density of states (DOS) at the fermi level and relative metallic bond strength (RMBS) of corresponding Pt-Ni-M' system. **e,** Correlation between E_{vac}, E_{hop}, E_a and RMBS. **f,** Schematic illustration of Sn-facilitated DOPT process.

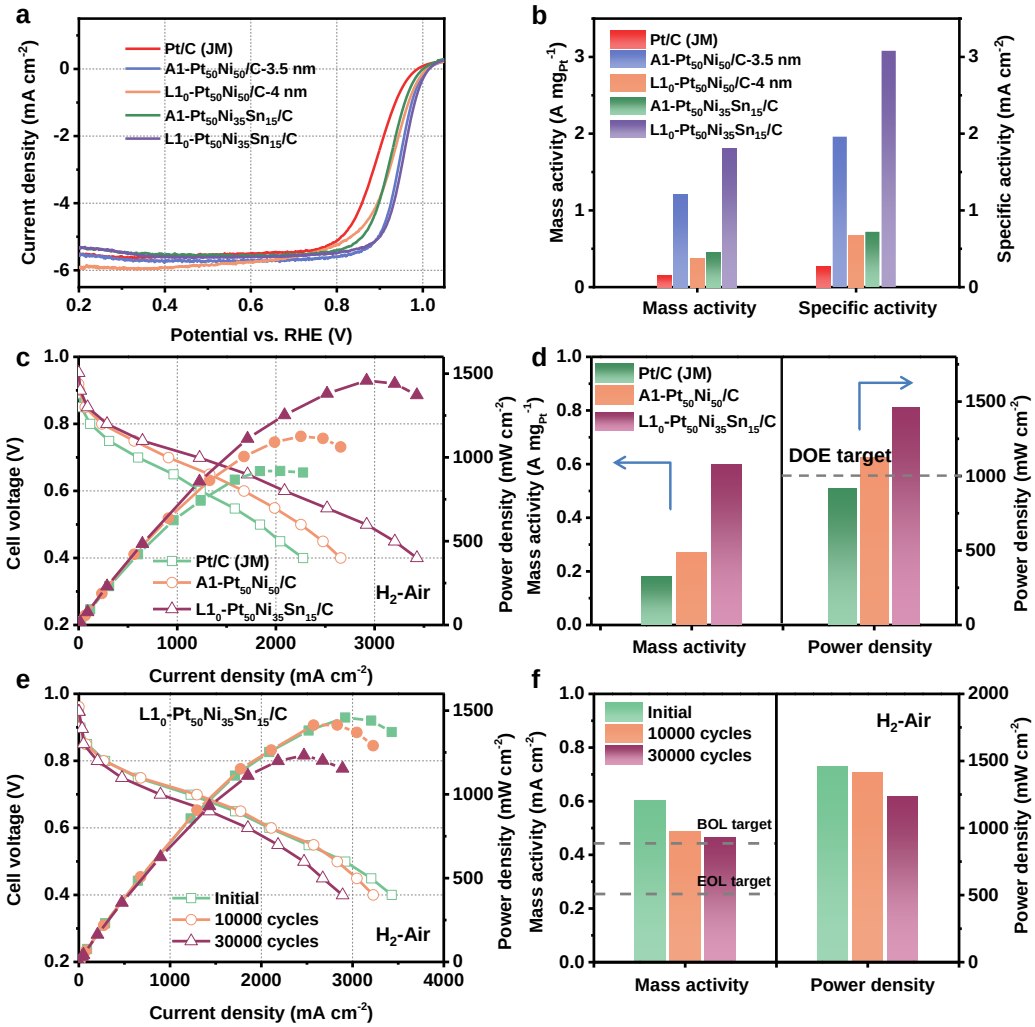

Fig. 5 | Electrochemical test and fuel cell performance of the studied catalysts. a, ORR polarization curves of Pt/C, A1-$Pt_{50}Ni_{50}$/C, L1$_0$-$Pt_{50}Ni_{50}$/C, A1-$Pt_{50}Ni_{35}Sn_{15}$/C and L1$_0$-$Pt_{50}Ni_{35}Sn_{15}$/C in O_2-saturated 0.1 M $HClO_4$ (rotating speed: 1600 rpm; scan rate: 10 mV/s). **b,** Relationship between $d_{Pt\text{-}Pt}$ and SA of the studied electrocatalysts. **c,** Fuel cell polarization curves of Pt/C, A1-$Pt_{50}Ni_{50}$/C and L1$_0$-$Pt_{50}Ni_{35}Sn_{15}$/C (H_2-Air). **d,** Comparison of MA and peak power density of Pt/C, A1-$Pt_{50}Ni_{50}$/C and L1$_0$-$Pt_{50}Ni_{35}Sn_{15}$/C. **e,** Fuel cell polarization curves and **f,** changes in MA and peak power density of L1$_0$-$Pt_{50}Ni_{35}Sn_{15}$/C before and after ADT tests.

Method

Synthesis of A1-$Pt_{50}Ni_{35}Sn_{15}$ NCs. In a typical synthesis, 10 mg $Pt(acac)_2$, 4.8 mg $Ni(acac)_2$ and 2.4 μL $Sn(Bu)_2(acac)_2$ were dissolved in 6 mL OAm. Under argon (Ar) atmosphere, the solution was stirred and degassed at 110 °C for 30 min. Subsequently, the temperature was raised to 280 °C at a rate of 5 °C min^{-1}, and maintained at this temperature for 1 h for complete reduction of Pt, Ni and Sn. Then, the solution it was cooled down to room temperature. Afterwards, the product was precipitated by adding ethanol, collected by centrifugation (9000 rpm, 15 min), washed three times with ethanol/hexane mixture, and then redispersed in hexane for further use. The preparations of $Pt_{50}Ni_{50-x}Sn_x$ NCs were similar except for change the molar ratio of Ni/Sn.

Synthesis of A1-$Pt_{50}Ni_{50}$ NCs. 10 mg $Pt(acac)_2$ and 6.5 mg $Ni(acac)_2$ were dissolved in 6 mL OAm. Under argon atmosphere, the solution was stirred and degassed at 110 °C for 30 min. Subsequently, the temperature was raised to 280 °C at a rate of 5 °C min^{-1} and kept at this temperature for 1 h before it was cooled down to room temperature. The purification process was similar with the preparation of $Pt_{50}Ni_{35}Sn_{15}$ NCs.

Loading NCs onto carbon. A certain amount of commercial carbon (Vulcan XC-72) was dispersed in 20 mL isopropanol/hexane under ultrasonication. After 30 min, the as-prepared NCs (for example, A1-$Pt_{50}Ni_{35}Sn_{15}$ NCs) dispersed in hexane were added dropwise. After ultrasonicating for another 1 h, the carbon supported NCs was separated by centrifugation, and washed with ethanol for 3 times. After drying in an oven under vacuum at 60 °C, the final product was obtained.

Synthesis of $L1_0$-$Pt_{50}Ni_{35}Sn_{15}$/C NCs. The as-prepared A1-$Pt_{50}Ni_{35}Sn_{15}$/C NCs were annealed at 450 °C under Ar + 5% H_2 for 1 h to prepare $L1_0$-$Pt_{50}Ni_{35}Sn_{15}$/C NCs.

Synthesis of $Pt_{50}M_{50-x}M'_x$ NCs (M = Fe/Cu/Zn, M' = In/Ga) and their phase transition. The synthetic protocols are similar with that of the preparation of A1-$Pt_{50}Ni_{35}Sn_{15}$ NCs, except for replacing Ni precursor by Fe/Cu/Zn precursor, replacing Sn precursor by In/Ga precursor. A desired molar ratio can be achieved by controlling the feeding ratio of Pt/M/M'. **Note:** For Pt-Zn and Pt-Cu systems, the reaction temperature and reaction time are 320 °C and 5 h, respectively. Under these conditions, Sn-doped $L1_0$-Pt-Zn and $L1_0$-Pt-Cu NCs can be obtained. For Pt-Fe system, the as-prepared M'-PtFe NCs were loaded onto carbon first, and then subjected to thermal annealing at 400 °C for phase transition.

Characterizations. TEM images were taken from a FEI Tecani G2 20 with an operation voltage of 200 kV. HRTEM and Scanning transmission electron microscopy (STEM) analyses were performed on a Hitachi HF-5000 with a probe aberration corrector. XRD were collected from Rigaku MiniFlex 600 diffractometer with a Cu radiation source (λ = 0.15406 nm).

The ordering degree (OD) is calculated according to the following equations:

$$\boldsymbol{OD}\ (\%) = \frac{S_{110}/S_{111}}{I^0_{110}/I^0_{111}} \quad (1)$$

$$\boldsymbol{OD}\ (\%) = \frac{S_{110}/(S_{111}+S_{200}+S_{002})}{I^0_{110}/(I^0_{111}+I^0_{200}+I^0_{002})} \quad (2)$$

Where S_{hkl} is the peak area of the obtained NCs, I_{hkl} is the peak intensify obtained from standard JCPDF card.

ICP-OES result was carried out from Agilent ICPOES 730. X-Ray Fluorescence (XRF) results were obtained from EAGLE III operated at 40 kV. Extended X-ray absorption fine structure spectroscopy (EXAFS) at the Pt L3-edge was performed at BL11B2 of Shanghai Beam Line. A Si (111) double-crystal monochromator was employed for the energy selection with resolution dE/E better than $2*10^{-4}$ at elemental edges. All XAS spectra were recorded at room temperature in transmission mode.

Electrochemical Measurements. Electrochemical measurements were performed on CHI760e electrochemical workstation (Shanghai Chenhua Instrument Corporation, China). Glassy carbon rotating disk electrode was employed as a working electrode (5 mm in diameter), Ag/AgCl (saturated

KCl) as a reference electrode and platinum plate (4 cm^2) as a counter electrode. All potentials were experimentally converted to values with reference to a reversible hydrogen electrode (vs. RHE).

The as-prepared catalysts (A1-$Pt_{50}Ni_{50}$/C, $L1_0$-$Pt_{50}Ni_{50}$/C, A1-$Pt_{50}Ni_{35}Sn_{15}$/C, $L1_0$-$Pt_{50}Ni_{35}Sn_{15}$/C, $L1_0$-$Pt_{50}Fe_{45}Sn_5$/C, $L1_0$-$Pt_{50}Cu_{45}Sn_5$/C, and $L1_0$-$Pt_{50}Zn_{40}Sn_{10}$/C) and commercial Pt/C were dispersed in a mixture containing water, isopropanol and Nafion (5%) (v/v/v = 1:1:0.1) to form a 2 mg mL^{-1} ink. 15 μL of ink was cast on the glassy carbon and dried under ambient condition. The final loading of the Pt was kept at 30-40 μg_{Pt} cm^{-2} (determined by ICP-OES).

The CV measurements were performed in N_2-saturated 0.1 M $HClO_4$ solutions at a scan rate of 50 mV/s after catalysts activation. The electrochemical active surface area (ECSA) was calculated by integrating the hydrogen underpotential deposition (H_{upd}) peak in CV, assuming 210 mC cm^{-2} for Pt NCs. The ORR polarization curves were recorded in O_2-saturated 0.1 M $HClO_4$ using a rotating disk electrode (RDE) at a rotation rate of 1600 rpm and a sweep rate of 10 mV s^{-1}. Mass activity and specific activity were calculated by normalizing kinetic current with mass loading and electrochemical surface area. Kinetic currents were calculated using Koutecky-Levich equation:

$$i_k = \frac{i_l * i_{0.9}}{i_l - i_{0.9}}$$

Where $\boldsymbol{i_k}$ is the kinetic current, $\boldsymbol{i_l}$ limiting current and $\boldsymbol{i_{0.9}}$ current at 0.9 V after *iR*-correction.

Accelerated durability test was performed at room temperature by applying cyclic sweeps between 0.6 and 1.0 V (vs. RHE) in O_2-saturated 0.1 M $HClO_4$ at a sweep rate of 100 mV s^{-1}**.**

MEA Preparation and Fuel Cell Testing. The obtained catalysts were homogeneously mixed with Nafion®, n-propanol, and water by ultrasonicating in an ice bath for 1 hour. Commercial Pt/C (40 wt.%) was adopted as the anode catalyst. The ink was then sprayed the ink onto Nafion® membrane (N211, active area 5 cm^2), with a catalyst loading of ~0.1 mg_{Pt} cm^{-2} for both anode and cathode (catalyst-coated membrane, CCM). The actual loading was determined by weighting the membrane before and after spraying.

The PEMFC tests were performed on Scribner 850e (Hephas Energy Corporation). Two gas diffusion layers (GDLs, thickness of 230 mm with a microporous carbon layer), two gaskets (PTFE layer with thickness of 200 mm), and the prepared CCM were assembled to prepare the MEA. The MEA was sandwiched between two graphite plates with single serpentine flow channels. Pure hydrogen and oxygen/air were supplied to the anode and cathode at gas flow rates of 200/500 and1000/2000 sccm (corresponding to stoich of 8-30 for cathode at voltage ≤ 0.6 V) with 100% relative humidity (RH). The cell was operated at 80 °C with a backpressure of 150 kPa_{abs} in H_2-O_2 condition and 250 kPa_{abs} in H_2-Air condition. Break-in process was performed at 0.5 V until a stable current was obtained. Rated power density is measured at 94 °C, 100% RH, 250 kPa_{abs}. Accelerated durability test (ADT) was performed by applying cyclic sweeps between 0.6 and 0.95 V (150 kPa_{abs}, H_2/N_2 100/100 sccm, 80°C, 100% RH).

DFT Calculations. Our spin-polarized first-principles computations were performed by using Vienna Ab initio Simulation Package (VASP)[33,34] with projector augment wave (PAW)[35,36] method and GGA-PBE[37-39] functional. Starting from the face-centered cubic (*fcc*) Pt crystal structure (2×2×2 supercell, 32 atoms), the disordered fcc Pt-Ni-M' systems were constructed by randomly replacing the Pt atoms with various numbers of Ni and M' atoms. Herein, the models $Pt_{16}Ni_{16}$, $Pt_{16}Ni_{14}M'_2$, $Pt_{16}Ni_{13}M'_3$, $Pt_{16}Ni_{11}M'_5$ were used, corresponding to the concentration of M' at 0%, 6.25%, 9.37% and 15.6%, respectively. The Pt-Ni-M' (M'=Sn, In, Ga) surfaces (100, 110, 111) were represented by a slab model with 4 atomic layers, where the top two layers were fully relaxed and the bottom two layers were fixed at the bulk lattice. The slab model was separated with a vacuum length of more than 15 Å. Atomic positions are optimized with the convergence of force less than 0.01 eV/Å with the electronic

relaxation threshold of 10^{-6} eV. Brillouin zone are sampled with 4×4×4, 4×4×1, 4×3×1 and 3×3×1 Gamma-centered k-points for bulk, (100), (110) and (111) surface, respectively. The climbing-image nudged elastic band (CI-NEB)[40] method and the improved dimer method (IDM)[41] were employed to search the minimum energy paths (MEP) and locate the transition states during the hoping process of Ni vacancy with the convergence of force of 0.05 eV/Å. Here, both in-plane (vacancy hoping on the first layer) and out-of-plane (vacancy hoping from the first layer to the second layer) hoping were taken into consideration, assuming that the vacancy is formed on the surface firstly.

The driving force (ΔE) from disordered structure transition to ordered structure was calculated with the following equation: $\Delta E = E(L_{10}) - E(fcc)$, where $E(system)$is the calculated energy of corresponding 'system'. The vacancy formation energy on the surface was estimated with the following equation: $E_{vac}(M, M = Pt, Ni, Sn, In, Ga) = E_{sur}(vac) + E(M) - E_{sur}(prinstine)$, where $E_{sur}(vac)$, $E(M)$, $E_{sur}(prinstine)$ are the energies of surface with vacancy, the atom of M in the pure bulk phase, and the surface without vacancy, respectively.

The free-electron picture suggested that metallic bond is the electrostatic force of attraction between the positive metal ions and the delocalized or free electrons. The three main factors that affect the strength of a metallic bond are: the number of delocalized electrons per atom (the more the stronger the bond), the atomic number of ions (the higher the atomic number the stronger the bond), and the size of the ions (the smaller the ion, the stronger the bond). Hence, we estimated the metallic bond strength (MBS) of Pt-Ni-M' systems with the following equation:

$$MBS(system) \propto \sum_{i=Pt,Ni,Sn,Ga,In} \frac{n_i \times N_{pi} \times N_e}{{r_i}^2}$$

Where n_i, N_{pi} and r_i are the number of 'i' atoms in the unit cell, the atomic number and atomic radius of 'i' atom, respectively. The N_e is the free electron or the delocalized electrons per atom. n_i, N_{pi} and r_i were obtained from atomic periodic table, and N_e is estimated from the band structure in Figure S5, where the bands cross the fermi level were account for the N_e. The free electrons estimated from the band structures are 32, 26, 22, 16, 22, 22 for $Pt_{16}Ni_{16}$, $Pt_{16}Ni_{14}Sn_2$, $Pt_{16}Ni_{13}Sn_3$, $Pt_{16}Ni_{11}Sn_5$, $Pt_{16}Ni_{11}In_5$, $Pt_{16}Ni_{11}Ga_5$, respectively. To compare the MBS of each Pt-Ni-M' system, using $Pt_{16}Ni_{16}$ as standard, the relative metallic bond strength (RMBS) was used as following:

$$RMBS(system) = {MBS(system)}\Big/{MBS(Pt_{16}Ni_{16})}$$

The calculated RMBS for $Pt_{16}Ni_{16}$, $Pt_{16}Ni_{14}Sn_2$, $Pt_{16}Ni_{13}Sn_3$, $Pt_{16}Ni_{11}Sn_5$, $Pt_{16}Ni_{11}In_5$, $Pt_{16}Ni_{11}Ga_5$ are 1.00, 0.82, 0.69, 0.50, 0.68, 0.69, respectively.

The oxygen binding energy E_O on (111) surface was defined as $E_O = E_{[surf + O]} - E_{[surf]} - E_{[O2]}/2$, where $E_{[surf + O]}$ and $E_{[surf]}$ are the total energies of the surface with and without the oxygen adsorbate, respectively. $E_{[O2]}$ is the total energy of an oxygen molecule.

Data availability

The data that support the findings of this study are available from the corresponding authors upon reasonable request. Source data are provided with this paper.

Code availability

The Vienna ab initio Simulation Package (VASP) for the density functional theory calculations is available at https://www.vasp.at.

33 Kresse, G. & Furthmuller, J. Efficient iterative schemes for ab initio total-energy calculations using a plane-wave basis set. *Phys. Rev. B* **54**, 11169 (1996).

34 Kresse, G. & Furthmüller, J. Efficiency of ab-initio total energy calculations for metals and

semiconductors using a plane-wave basis set. *Comp. Mater. Sci.* **6**, 15-50 (1996).
35 Blochl, P. E. Projector augmented-wave method. *Phys. Rev. B* **50**, 17953-17979 (1994).
36 Kresse, G. & Joubert, D. From ultrasoft pseudopotentials to the projector augmented-wave method. *Phys. Rev. B* **59**, 1758 (1999).
37 Perdew, J. P., Burke, K. & Ernzerhof, M. Generalized Gradient Approximation Made Simple. *Phys. Rev. Lett.* **78**, 1396-1396 (1997).
38 Perdew, J. P., Ernzerhof, M. & Burke, K. Rationale for mixing exact exchange with density functional approximations. *J. Chem. Phys.* **105**, 9982-9985 (1996).
39 Perdew, J. P., Burke, K. & Ernzerhof, M. Generalized Gradient Approximation Made Simple. *Phys. Rev. Lett.* **77**, 3865-3868 (1996).
40 Henkelman, G., Uberuaga, B. P. & Jo´nsson, H. A climbing image nudged elastic band method for finding saddle points and minimum energy paths. *J. Chem. Phys.* **113**, 9901-9904 (2000).
41 Heyden, A., Bell, A. T. & Keil, F. J. Efficient methods for finding transition states in chemical reactions: Comparison of improved dimer method and partitioned rational function optimization method. *J. Chem. Phys.* **123**, 224101 (2005).

Acknowledgments: This work is supported by the National Key Research and Development Program of China (grant 2021YFA1501001), National Nature Science Foundation of China (grant 22122202, 21972051, 52025133) and NSF-PREM program (grant DMR-1828019). *In-situ* STEM experiments were carried out on Hitachi HF-5000 and the authors appreciate the help from Mr. Matsumoto from Hitachi. The authors thank the Analytical and Testing Center of Huazhong University of Science and Technology (HUST) for carrying out the TEM, XRF, and XRD measurements.

Author contributions: Q.L. and S.J.G. conceived the idea and designed the experiments. J.S.L, X.L, S.Z.L., F. L., Y.J.S. carried out the sample synthesis, characterization, and measurements. H.F.L. and G.X.W. performed the *in-situ* XRD measurements. J.X., Z.D. and J.T.H. performed the PDF tests. Y.Y.W., J.Y.L. and G.L. provided theoretical calculations. J.S.L. performed the fuel cell measurements. J.S.L., Q.L., Y.H.H., and S.J.G. wrote and revised the manuscript. All the authors contributed to the overall scientific discussion and edited the manuscript.

Competing interests: Authors declare that they have no competing interests.

Additional information

Supplementary information The online version contains supplementary material available at https://doi.org/10.1038/s41586-021-04068-z.

Correspondence and requests for materials should be addressed to Qing Li or Shaojun Guo.